

# Towards Scalable Production of Sodium-Ion Batteries: Solvent-Free Layered-Oxide Cathodes and Aqueous-Processed Hard Carbon Anodes for Cost-Effective Full-Cell Manufacturing

Johannes Kühn,<sup>[a, b]</sup> Florian Schmidt,<sup>[b]</sup> Pascal Seete,<sup>[a, b]</sup> Tom Boenke,<sup>[b]</sup> Florian S. Hoffmann,<sup>[b]</sup> Arthur Dupuy,<sup>[b]</sup> Benjamin Schumm,<sup>[b]</sup> Thomas Abendroth,<sup>[b]</sup> Holger Althues,\*<sup>[b]</sup> and Stefan Kaskel<sup>[a, b]</sup>

Achieving commercial viability for more sustainable sodium-ion batteries (SIB) necessitates reducing the environmental impact of production, particularly originating from electrode drying and the use of toxic solvents like N-methyl-2-pyrrolidone (NMP). This study presents the dry-processing of commercial P2-type  $\text{Na}_{0.75}\text{Ni}_{0.25}\text{Fe}_{0.25}\text{Mn}_{0.50}\text{O}_2$  (NFM) via the DRYtraec® process, aiming to lower the binder content of 1 wt.% polytetrafluoroethylene (PTFE) and eliminating the need for electrode drying and NMP recovery. Assessments of electrode morphology and active material crystallinity were conducted to gauge the effects of mechanical stress during processing. The resulting cathodes, loaded at a commercially relevant  $2.3\text{--}2.7 \text{ mAh cm}^{-2}$  loading,

were successfully paired with aqueous-processed hard carbon (HC) anodes, demonstrating stable performance in full-cells. Comparative analysis with entirely wet-processed electrodes revealed comparable capacity accessibility and comparable long-term stability. This showed the competitiveness of dry-processed cathodes. Finally, the integration of NMP-free, dry-processed cathodes and aqueous-processed anodes was scaled to the commercially relevant prototype pouch-cell. The cell demonstrates stable cycling for 400 cycles with an energy density of  $102 \text{ Wh kg}^{-1}$  as well as reduced processing costs and environmental footprint.

## 1. Introduction

Decarbonizing the world economy is an essential future target in the 21<sup>st</sup> century requiring energy from renewable energy sources. However, the fluctuation of wind and solar power and the transformation to electrified mobility pose an increasing demand for energy storage technologies.<sup>[1–3]</sup> In addition to a high energy density, these storage technologies should be reliable, safe, environmentally friendly, and cost-efficient.<sup>[4]</sup> In recent years, lithium-ion batteries (LIB) become the dominant technology that fulfills a part of these requirements, namely a high energy density, sufficient safety, and cost-efficiency.<sup>[2,5]</sup> However, their cost advantage is strongly related to the prices of the raw materials incorporated in the cell. As the demand for

LIB increases, especially due to the growth of the electric vehicle (EV) market, raw material costs will increase accordingly.<sup>[1]</sup> Besides low abundant critical active materials based on nickel or cobalt that could be replaced by lithium iron phosphate (LFP) or sulfur,<sup>[6,7]</sup> total global reserves are limited with respect to lithium to approximately 26 million tons (resources 98 million tons).<sup>[8]</sup> Therefore, the lithium price will further increase as a result of the continuous growth of energy storage demand, except when replacing the charge carrier lithium with another metal, such as sodium.<sup>[9]</sup> In a sodium-ion battery (SIB) the charge is transferred between both electrodes by sodium ions.<sup>[10]</sup> While the drawbacks of SIB are still lower energy densities and a more complex intercalation mechanism in the cathode,<sup>[11–13]</sup> the interest in this cell system increased in recent years.<sup>[14–17]</sup> A major reason is the fact that the sodium prices are significantly lower than the lithium prices, as sodium abundance exceeds the one of lithium by three orders of magnitude.<sup>[14]</sup> Additional cost-savings are related to the replacement of the copper anode current-collector by aluminium.<sup>[18]</sup> Furthermore, it is estimated that SIB reveal advantages in terms of carbon- and water-footprint with respect to LIB or Li–S batteries.<sup>[19]</sup> At the current state, lower energy densities of SIB are outbalancing cost savings from sodium raw material price and current collector replacement, leading to a higher material and energy demand per kWh storage as well as higher production cost.<sup>[18]</sup> Hence, the manufacturing process of cells becomes the major contributor to cost per kWh.

[a] J. Kühn, P. Seete, S. Kaskel  
Technische Universität Dresden, Chair of Inorganic Chemistry I, Bergstraße 66, 01069 Dresden, Germany

[b] J. Kühn, F. Schmidt, P. Seete, T. Boenke, F. S. Hoffmann, A. Dupuy, B. Schumm, T. Abendroth, H. Althues, S. Kaskel  
Fraunhofer Institute Materials and Beam Technology, Winterbergstraße 28, 01277 Dresden, Germany  
E-mail: holger.althues@iws.fraunhofer.de

 Supporting information for this article is available on the WWW under <https://doi.org/10.1002/batt.202400572>

 © 2025 The Author(s). *Batteries & Supercaps* published by Wiley-VCH GmbH. This is an open access article under the terms of the Creative Commons Attribution License, which permits use, distribution and reproduction in any medium, provided the original work is properly cited.

To address these current limitations, the contribution of production and environmental footprint are faced by switching from solvent-assisted electrode coating to solvent-free coating as a promising opportunity.<sup>[20,21]</sup> Solvent-free coating does not require (toxic) solvents, such as N-methylpyrrolidone (NMP), in the electrode production chain which is part of the current state-of-the-art manufacturing for LIB as well as SIB.<sup>[22,23]</sup> Thereby, the energy consumption of the electrode coating process could be reduced by 75–85%,<sup>[20]</sup> as no drying and solvent recovery steps are necessary. Since these production steps become redundant, the initial investment required for production plants is lower as well. Additionally, the dry coating step reduces the footprint of the plant by 15–30%,<sup>[20]</sup> enabling a further reduction of the investment cost. An especially promising dry coating approach is the dry transfer electrode coating process or DRYtraec®, as it allows the facile and solvent-free fabrication of dry electrodes without handling delicate free-standing films.<sup>[20,24,25]</sup> Previously, it was demonstrated that this coating process is compatible with a wide variety of active materials, ranging from graphite over  $\text{Li}_a\text{Ni}_x\text{Mn}_y\text{Co}_z\text{O}_2$  to next-gen materials such as sulfur, and even solid electrolytes by several groups.<sup>[21,26–30]</sup>

In this work, we applied this cost-efficient coating technique to fabricate solvent-free cathodes for SIB with ultra-low binder content and reduced footprint, reported for the first time. Therefore, the active material, layered transition metal oxide  $\text{Na}_{0.75}\text{Ni}_{0.25}\text{Fe}_{0.25}\text{Mn}_{0.50}\text{O}_2$  cathode (NFM) was selected due to its high potential with respect to abundant precursors as well as a high specific capacity of up to 208 mAh g<sup>-1</sup>.<sup>[31]</sup> A characterization using scanning electron microscopy (SEM) and X-ray diffraction (XRD) before and after DRYtraec® processing is performed to evaluate the impact of the coating routine on the active material. The as-prepared NFM cathodes as well as wet-based hard carbon anode (HC) are electrochemically evaluated using a carbonate-based electrolyte (ethylene/diethylene carbonate, EC/DEC with 1 M NaPF<sub>6</sub>) at half-cell level and compared to a wet-processed analogue, afterwards. Finally, the combination of processed electrodes in full-cells is investigated at coin-cell and pouch-cell level including postmortem analysis.

## 2. Results and Discussion

Cathodes were fabricated using commercially available NFM material and 1 wt.% binder through the solvent-free DRYtraec® process and NMP-based wet-processing methods. HC anodes

were prepared with an aqueous-processing approach. The resulting cathodes and anodes reveal areal capacities exceeding 2.3 mAh cm<sup>-2</sup> as characterized in Table 1.

### 2.1. Surface Morphology of Dry-Processed Layered Oxide Cathodes

NFM-based cathodes were characterized using SEM and focused ion beam SEM (FIB-SEM), as shown in Figure 1. The applied processing method affects the active material morphology, with pristine NFM-particles displaying intertwined plate-shaped lamellae (Figure S 1d–f), while the cathode surface particles appear flattened (Figure 1c). The presence of PTFE-fibrils is visible in Figure 1c, connecting NFM agglomerates whereas carbon additives fill the spaces between particles, forming a good percolation network (Figure 1e).

The FIB-SEM cross-section of the dry-cathode in Figure 1d shows a gradient in densification, with higher compaction at the electrode surface and lower compaction in the bulk. A comparison between Figure 1f and Figure S 1e confirms that the NFM particle morphology within cathode bulk remains largely intact. This densification gradient suggests that NFM particles experience flattening primarily in the direct contact zone between the roller and the composite.

This effect can be attributed to two factors. First, increased heat impact at the roller during the lamination step might be linked to particle deformation as the powder film is pressed onto the current collector foil. Second, lamination introduces two distinct mechanical forces: a static force exerted by the roller carrying the powder film and a shear force applied by the second roller transporting the current collector. The interaction of these forces result in plastic deformation of particles, leading to cracking, flattening, or reorganization while maintaining the overall morphology. This behavior is comparable to the effects observed in electrode calendering.<sup>[32]</sup>

A high suitability of the DRYtraec® process was concluded from a promising film-formation (Figure S 2) and a retained particle shape inside the electrode bulk. However, a deformation of the NFM particles at the cathode surface requires the investigation of crystallinity and electrochemical performance as performed in the following sections.

**Table 1.** Properties of prepared electrodes by dry-processing (Dry) and wet-processing (Slurry) based on the values from half-cell, full-cell, and pouch-cell electrodes.

Label	AM content [wt.%]	Binder	Binder content [wt.%]	Areal loading [mg cm <sup>-2</sup> ]	Areal capacity [mAh cm <sup>-2</sup> ]	Electrode density [g cm <sup>-3</sup> ]	Adhesion strength [kPa]
NFM <sub>Dry</sub>	96	PTFE	1	20.2–22.7	2.4–2.7	1.8	53
NFM <sub>Slurry</sub>	96	PVDF				1.3	128
HC <sub>Slurry</sub>	90	SBR	5	7.4–9.3	2.4–3.0	0.7	–

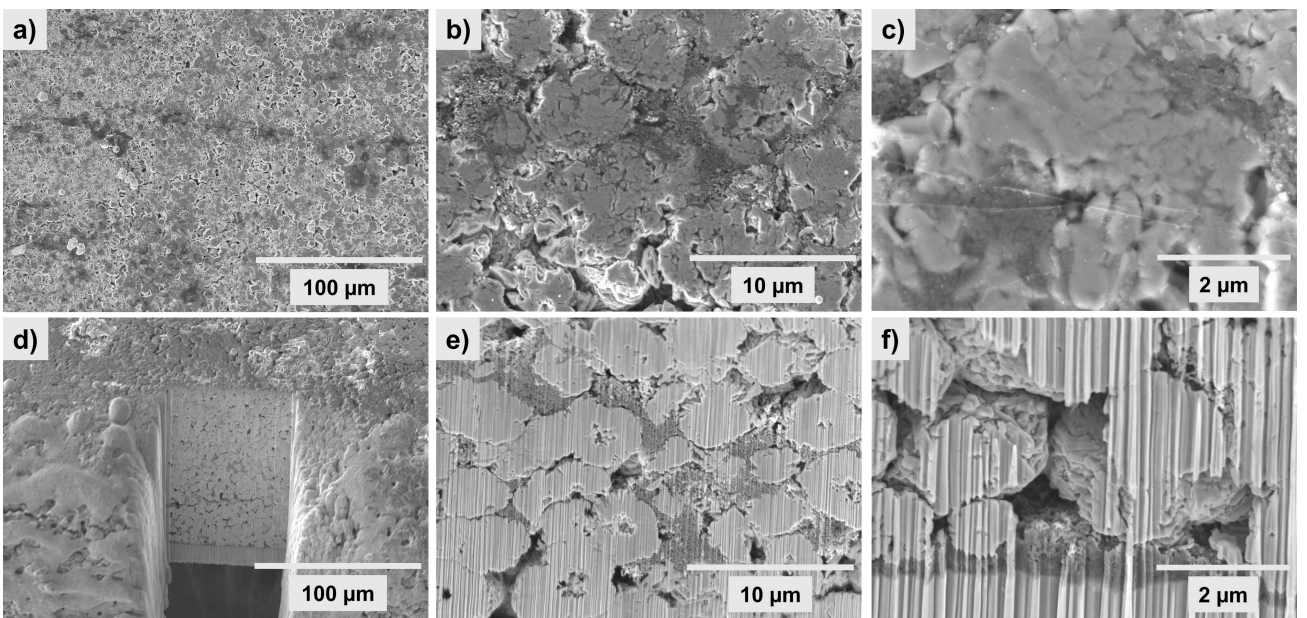


**Figure 1.** SEM micrographs (a–c) of NFM-based dry-film cathodes produced via DRYtraec® as well as the corresponding FIB-SEM micrographs (d–f) of the electrode cross-section.

## 2.2. Influence of Processing on the Cathode Active Material Crystallinity

XRD analysis in reflective Bragg-Brentano geometry was performed on pristine NFM powder and as-prepared DRYtraec® cathodes to assess any adverse effects on the NFM crystalline structure. From the comparison of diffractograms, a material degradation would be detectable by emerging amorphous material contributions as well as changes in inter-layer spacing by water intercalation.<sup>[33]</sup> Both investigated samples of  $\text{Na}_{0.75}\text{Ni}_{0.25}\text{Fe}_{0.25}\text{Mn}_{0.50}\text{O}_2$  exhibited P2-type layered structures with a space group of  $\text{P}6_3/\text{mmc}$  (Figure S 4).<sup>[34]</sup> Detailed NFM crystalline structure and lattice parameters were reported previously by Lan et al.<sup>[34]</sup> and Chen et al.<sup>[35]</sup>

In Figure S 4, no amorphous contribution or change in interlayer spacing were observed between pristine NFM and NFM within processed cathodes, suggesting that dry-processing under nitrogen atmosphere had no significant impact on the composition or crystal structure of the layered oxide. However,  $\alpha\text{-Fe}_2\text{O}_3$  signals at  $41^\circ$  and  $68^\circ$  within the pristine materials and the processed electrode, suggest potential contamination or unfavorable synthesis condition by the producer.<sup>[36]</sup>

## 2.3. Three-Electrode Cell Measurement at Half-Cell Level

Initial tests in half-cells are performed to assess specific capacities of dry and aqueous processed cathodes and to compare voltage curves. Processed HC and NFM electrodes were assembled as the working electrode in three-electrode half-cells, with a sodium metal counter electrode and sodium metal reference. This cell configuration was chosen to mitigate reported sodium overpotential.<sup>[37,38]</sup>

From Figure 2a, a comparable cathode charging capacity of  $119 \text{ mAh g}^{-1}$  during the first formation cycle between  $2.0\text{--}4.1 \text{ V}$  highlights a good comparability between both electrodes. Moreover, no deviation in addressable capacity is noted from half-cell results, suggesting no active material damage or delamination during surface compaction during the DRYtraec® process as identified in section 2.1. The dQ/dV diagrams (Figure 2c, d) allow a comparison of respective capacity contributions. In Figure 2b, cathodic capacity contributions within two regimes could be identified for both cathode types, namely  $2.7\text{--}4.0 \text{ V}$  and  $>4.0 \text{ V}$ . A identification of the capacity contributions to  $\text{Mn}^{3+}/\text{Mn}^{4+}$  at  $2.1 \text{ V}/2.0 \text{ V}$ ,  $\text{Ni}^{2+}/\text{Ni}^{3+}$  at  $3.7 \text{ V}/3.6 \text{ V}$  and  $\text{Ni}^{3+}/\text{Ni}^{4+}$  as well as  $\text{Fe}^{2+}/\text{Fe}^{3+}$  for a voltage higher than  $4.0 \text{ V}$  was performed on basis of the reported P2-type  $\text{NaNi}_{0.15}\text{Fe}_{0.20}\text{Mn}_{0.65}\text{O}_2$  cathode material by Yuan et al.<sup>[39]</sup> Notably, a higher structural stability is expected due to a broader capacity contribution at  $2.7\text{--}3.4 \text{ V}$  of the investigated  $\text{Na}_{0.75}\text{Ni}_{0.25}\text{Fe}_{0.25}\text{Mn}_{0.50}\text{O}_2$  in comparison to the reported  $\text{NaNi}_{0.15}\text{Fe}_{0.20}\text{Mn}_{0.65}\text{O}_2$  with a lower nickel content.<sup>[39,40]</sup> A shift of voltage curve after the first cycle by  $6 \text{ mAh g}^{-1}$  was related to the selected lower voltage limit of  $2 \text{ V}$  resulting in a partial sodiation of open vacancies of the P-type layered transition metal oxide.<sup>[41]</sup> Latter is only present in half-cells against sodium counter-electrode and cannot be utilized in full-cells leading to the selection of first cycle charging capacity for full-cell balancing of the cathode.

The HC<sub>slurry</sub> anode (Figure 2c) showed an initial discharging capacity (sodiation) of  $323 \text{ mAh g}^{-1}$  (ICE: 85.9%) at  $0.05 \text{ C}$ , with continuous cycling resulting in a reversible capacity of  $273 \text{ mA g}^{-1}$  (CE: 98.8%). A plateau at  $0.7 \text{ V}$  (Figure 2c) can be attributed to the oxidation of FEC additive, used for stabilizing the sodium metal counter electrode, emphasized in the dQ/dV plot (Figure 2d).<sup>[42]</sup>

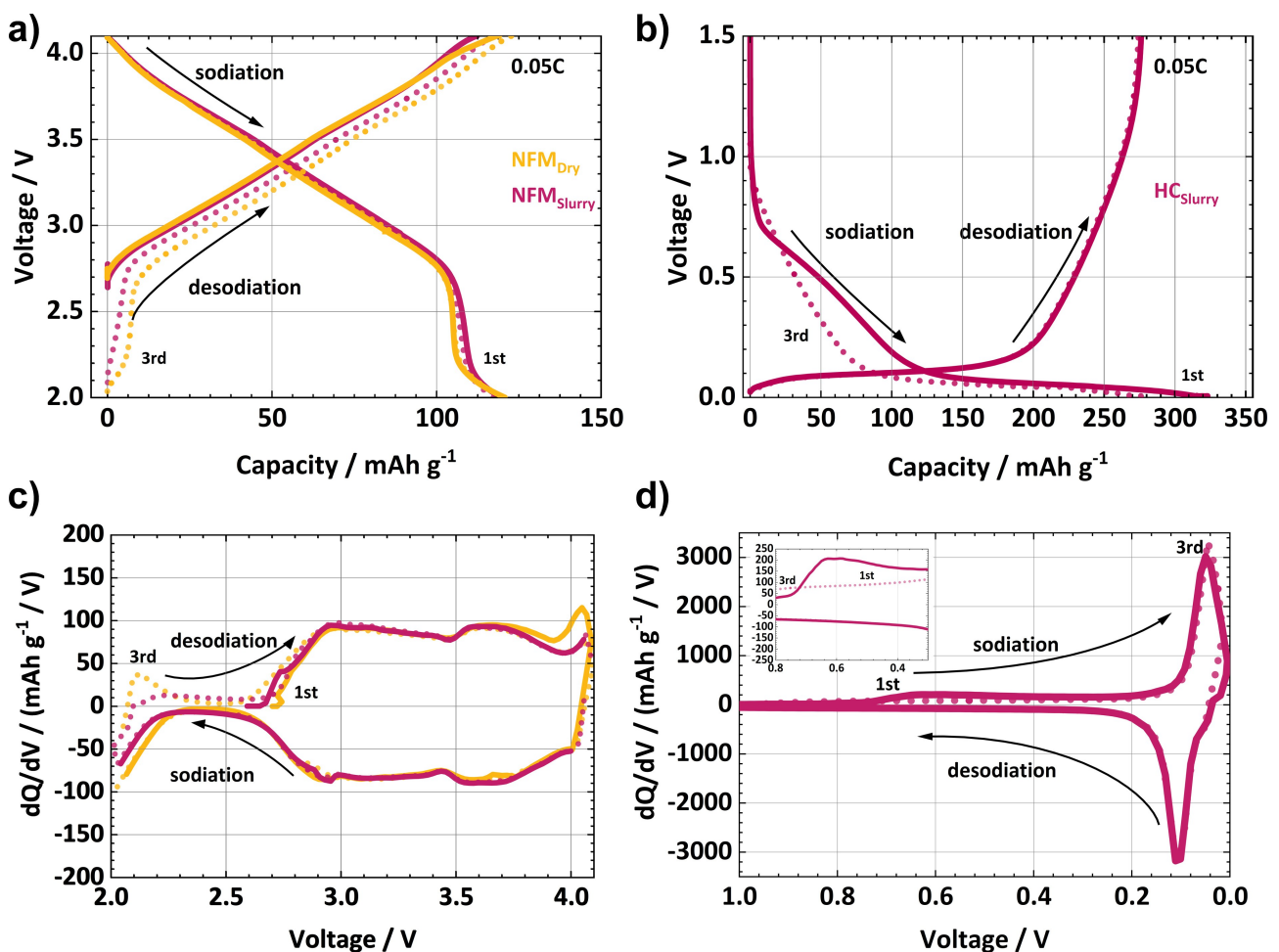


**Figure 2.** Resulting voltage profiles from three electrode half-cell measurements of NFM<sub>Dry</sub> and NFM<sub>Slurry</sub> with corresponding differential voltage plot dQ/dV (a, c). The hard carbon anode voltage profile as well as the differential voltage plots (b, d). Dotted graph indicates 3rd cycle.

First cycle discharging capacity of the HC anode was selected for full-cell balancing.

#### 2.4. Electrochemical Characterization at Full-Cell Level

##### 2.4.1. Comparison on Coin-Cell Level

The Full-cell performance of NFM<sub>Dry</sub> vs. HC<sub>Slurry</sub> was compared by measuring NFM<sub>Slurry</sub> vs. HC<sub>Slurry</sub> for an N/P ratio of 1.0 in a voltage window of 4.1–1.5 V. A comparability to half-cell results was achieved by the selected N/P ratio with respect to the voltage shift in full-cells as shown in Figure S 7. The cells were cycled after an initial formation at 0.05 C from 0.1 C towards 3 C during an asymmetrical rate capability test. Latter was extended by continuous cycling until 124 cycles at 0.5 C as illustrated in Figure 3 and three cycles of 0.1 C to compare the changes in voltage contribution.

Specific discharge capacities of 100 mAh g<sup>-1</sup> (ICE: 83.4%, C<sub>s, charge</sub>: 120 mAh g<sup>-1</sup>) and 98 mAh g<sup>-1</sup> (ICE: 86.1%, C<sub>s, charge</sub>: 114 mAh g<sup>-1</sup>) were obtained for NFM<sub>Dry</sub> vs. HC<sub>Slurry</sub> and NFM<sub>Slurry</sub> vs. HC<sub>Slurry</sub> configuration, respectively (Figure 3a). A good agree-

ment with the half-cell measurements in three-electrode setup is indicated by a comparable charge capacity. The lower ICE of SIB full-cells (83–86%) compared to half-cells (~90%) is widely reported and was related to trapped capacity within the HC anode in Na<sub>3</sub>V<sub>2</sub>PO<sub>4</sub>/HC full-cells.<sup>[43,44]</sup>

The continuous cycling at 0.1 C as well as the voltage curves of the rate performance test until 2 C, depicted in Figure 3a and Figure 3b, reveal slightly higher values for the full-cell capacity in comparison to wet-processed cathodes showing comparable active material utilization. In detail 89% (0.5 C) and 81% (2 C) of the initial discharge capacity (0.05 C) were accessible. A further increase in C-rate towards 3 C revealed a difference in rate capability between 50% for NFM<sub>Dry</sub> and 78% for NFM<sub>Slurry</sub> indicating a reduced active material utilization. These observations might relate to a difference in compaction during electrode preparation which is evident by the density 1.8 g cm<sup>-3</sup> and 1.3 g cm<sup>-3</sup> for dry-processed and wet-processed cathodes. A difference in ionic transport resistance is therefore expected based on the SEM images and difference in rate capability. Hence, higher currents reveal a limitation by ionic diffusion within the dry-processed cathode as already described for Na<sub>3</sub>V<sub>2</sub>(PO<sub>4</sub>)<sub>3</sub>.<sup>[32,45]</sup>

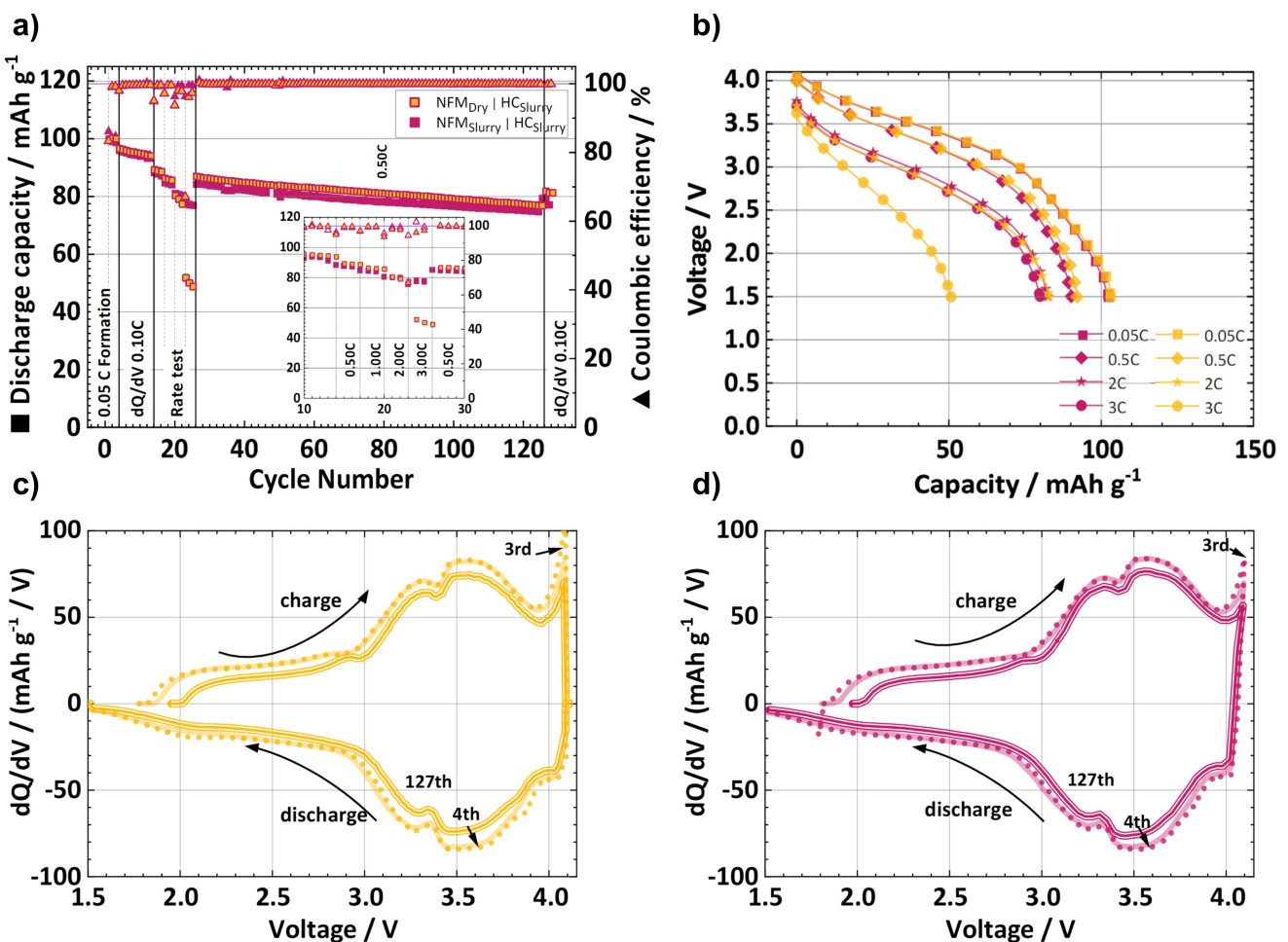


**Figure 3.** Discharge capacities of full-cells assembled from processed cathodes NFM<sub>Dry</sub> and NFM<sub>Slurry</sub> against HC<sub>Slurry</sub> (a) as well as voltage curves from the third cycle of each current rate during the rate capability test. (b). Impact of rate-capability test as well as long-term cycling are illustrated in dQ/dV plots of respective cycles for NFM<sub>Dry</sub> vs. HC<sub>Slurry</sub> (c) and NFM<sub>Slurry</sub> vs. HC<sub>Slurry</sub> (d) at 0.1 C.

During subsequent cycling until 124<sup>th</sup> cycle, a 9% decay in capacity from 87 mAh g<sup>-1</sup> for NFM<sub>Dry</sub> and 84 mAh g<sup>-1</sup> for NFM<sub>Slurry</sub> was found during 100 cycles at 0.5 C. A final CE value for the 124<sup>th</sup> cycle was found to be 99.89% and 99.97% for NFM<sub>Dry</sub> and NFM<sub>Slurry</sub>, respectively. Hence, continuous cycling results in a comparable capacity decay whereas a lowered CE of NFM<sub>Dry</sub> hints towards capacity losses related to a constant leak of charges. A reformation of the solid electrolyte interface (SEI) should be considered due to the increased roughness of electrode surface found from cathodes extracted by post mortem analysis shown in Figure S 7. From dQ/dV plots in Figure 3c and Figure 3d, a comparable decay of each capacity contribution was measured. The comparison of the 3<sup>rd</sup> and 127<sup>th</sup> cycle shows a constant reduction of peak intensities for charge and discharge as well as a shifting of peaks towards higher voltage for charge. An in-depth DVA of full-cell degradation is out of the scope of this work, but a trend for increasing cell resistance was identified according to literature.<sup>[32,46]</sup>

This increase in cell overpotentials agrees with a fast decay in capacity contribution over initial cycles for the contribution of Ni<sup>3+</sup>/Ni<sup>4+</sup> as well as Fe<sup>2+</sup>/Fe<sup>3+</sup> close to the upper voltage limit

at 4.1 V identified in section 3.3. An increase of resistance due to sodium metal plating was excluded from further consideration due to the lack of evidence from post-mortem analysis depicted in Figure S 7b.

A comparable capacity decay of 9% (0.5 C) during continuous cycling as well as a decrease of each capacity contribution in the dQ/dV plots showed a comparable degradation of full-cell capacity on coin-cell level, irrespective of the type of cathode. The difference in rate capability depending on the electrode processing was identified and was explained by the process-related impact of electrode densification leading to a difference in ionic transport resistance.

#### 2.4.2. Investigation in Pouch-Cells

Prototype single-layer pouch-cells were evaluated for rate capability, long-term cycle life as well and energy density calculations on stack-level. Therefore, dry-processed cathodes were combined with wet-processed hard carbon anodes. An increase in N/P ratio towards 1.1 is recommended to avoid risk

of sodium metal plating due to a higher electrode surface area that could be prone to inhomogeneity in areal capacity. Initial discharge capacities of measured cells are  $106 \text{ mAh g}^{-1}$  (ICE: 85.2%,  $C_{s, \text{charge}}$ :  $124 \text{ mAh g}^{-1}$ ) for  $2.7 \text{ mAh cm}^{-2}$  and  $101 \text{ mAh g}^{-1}$  (ICE: 84.6%,  $C_{s, \text{charge}}$ :  $119 \text{ mAh g}^{-1}$ ) for  $2.4 \text{ mAh cm}^{-2}$  (Figure 4a). These values agree with a charge capacity of  $119 \text{ mAh g}^{-1}$  determined from three-electrode half-cell measurements of section 3.3 and full-cells on coin-cell level in section 2.4.1. With respect to cycle life, the upper voltage limit was decreased from 4.1 V towards 4.0 V to account for the increase in N/P ratio compared to section 3.4.1. An asymmetric rate test was conducted to verify the accessible capacity for discharge rates from 0.1 C towards 2 C. An emerging deviation can be found with increasing C-rate resulting in slightly higher capacity values for the lower loaded electrodes. Again a limitation of ionic diffusion can be expected as observed for the comparison of rate capability between high density dry-processed cathodes and wet-processed cathodes on coin-cell level in section 2.4.1.

From long-term cycling to 400 cycles, a capacity decay of  $19.3 \text{ mAh g}^{-1}$  or 26% ( $\text{CE}_{400\text{th}}$ : 99.75%) and  $15.6 \text{ mAh g}^{-1}$  or 23% ( $\text{CE}_{400\text{th}}$ : 99.89%) were derived for a cathode loading of  $2.7 \text{ mAh cm}^{-2}$  and  $2.4 \text{ mAh cm}^{-2}$ , respectively. A detailed distribution of CE values from Figure 4b, reveals a more stable CE of  $> 99.9\%$  for electrodes with lower areal loading whereas higher loadings seem to cause fluctuating CE values between 99.7–99.9% resulting in an accelerated degradation of the cell.

A maximum specific energy of  $102 \text{ Wh kg}^{-1}$  and an energy density of  $139 \text{ Wh L}^{-1}$  were calculated on stack-level for initial cycles with an average voltage of 3.3 V and  $70.7 \text{ mAh}$  capacity for cells with a cathode loading of  $2.7 \text{ mAh cm}^{-2}$ . From literature a specific energy of up to  $165 \text{ Wh kg}^{-1}$  was reported based on layered oxide cathode and HC anode.<sup>[11,47]</sup> With respect to further energy density optimization, which was not in the scope of this work, lower electrolyte amounts need to be tested. For the reported cells, a mass contribution of 49% from

the electrolyte was estimated. Calculations on the electrode porosity by Equation S 1 and Equation S 2 showed an excess of electrolyte of 263% based on 1 ml ( $14 \mu\text{L mAh}^{-1}$ ) electrolyte with respect to the available electrode pore volume. An excess of 150% ( $0.57 \text{ ml} | 8 \mu\text{L mAh}^{-1}$ ) of the electrode porosity was selected for possible application from LIB<sup>[48]</sup> which would lead to a specific energy of  $130 \text{ Wh kg}^{-1}$  ( $184 \text{ Wh L}^{-1}$ ). Therefore, the optimization of electrode densities, electrolyte amount<sup>[48]</sup> and loading<sup>[49]</sup> towards high energy multi-layer pouch-cells are planned.

With respect to cell degradation, post-mortem analysis on anode and cathode were conducted using SEM measurements on FIB cuts and energy dispersive X-ray spectroscopy (EDX) after 400 cycles. The comparison of cathodes before and after cycling (Figure 5) reveals a slight increased inter-particular spacing within the electrode bulk. In contrast, the interface between electrode coating and primed current collector in Figure 5 c,d does not indicate the appearance of particle-delamination. To take into account, the lower adhesion strength of the derived dry-processed cathodes from Table 1 and higher reported elasticity of PTFE compared to PVDF, the swelling of the electrodes should be expected.<sup>[29,50]</sup>

From Figure 6b, the FIB cut of the anode reveals a  $50 \mu\text{m}$  thick sodium layer on the surface as well as a coating of active material particle identified as SEI within the electrode bulk (Figure 6c). The EDX graphs in Figure 6d–h show a particle coating out of sodium oxide as well as cathode metal species such as Mn, Fe and Ni. The presence of sodium oxide is caused by the contact to atmosphere during transport.

As described by Che et al., the dissolution and migration of NFM cathode material species in  $1 \text{ M NaPF}_6$  in propylene carbonate (PC) and ethyl methyl carbonate (EMC) towards the anode might cause sodium metal plating.<sup>[51]</sup> The presence of sodium metal plating on the anode including cathode active material species confirms a comparable dissolution of the

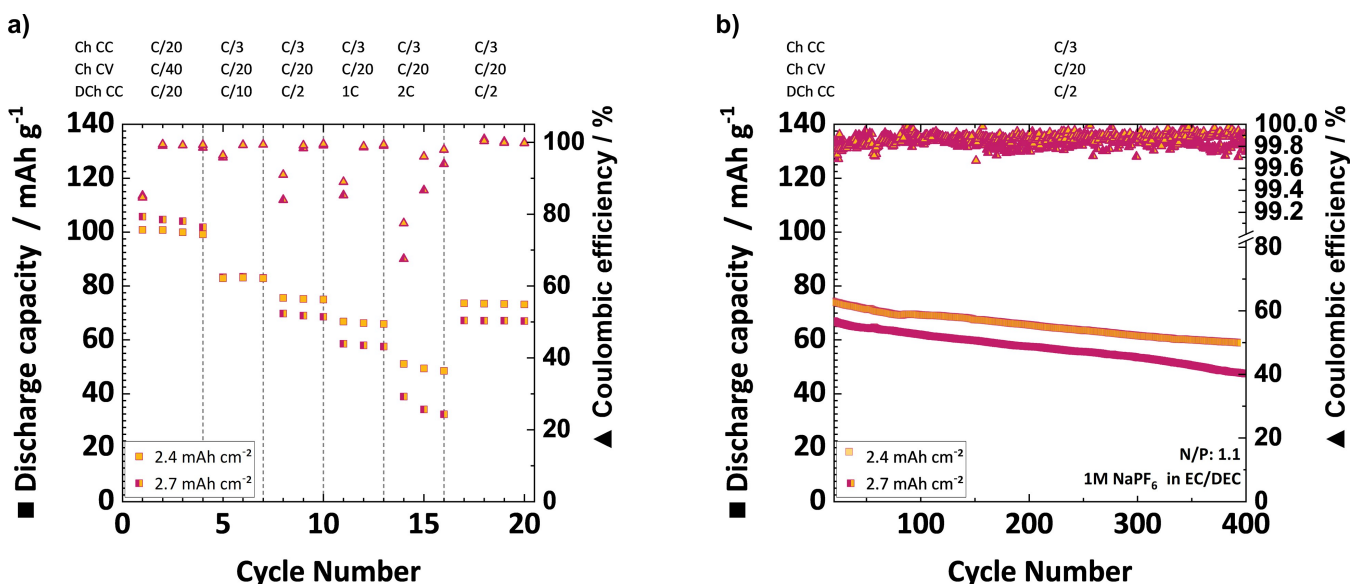
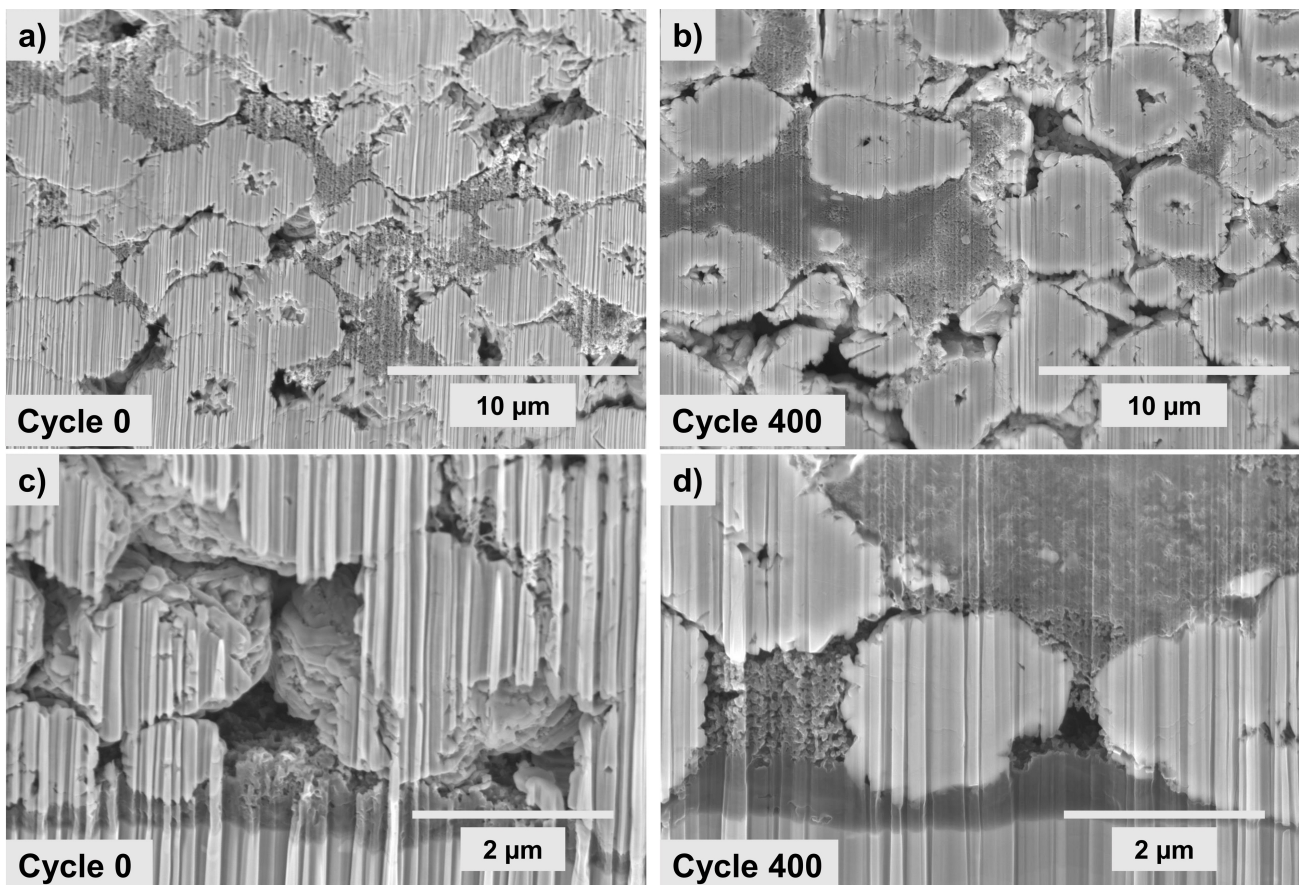


Figure 4. Discharge capacities as well as CE for single layer pouch-cells based on  $\text{NFM}_{\text{dry}}$  vs.  $\text{HC}_{\text{Slurry}}$  for different loadings (a) as well as long-term cycling results up to 400 cycles (b).



**Figure 5.** SEM micrograph of dry-processed cathode in pristine form and extracted after 400 cycles. (a, b) comparison of electrode bulk and (c, d) current collector interface.

investigated NFM in 1 M NaPF<sub>6</sub> in EC/DEC. Herein, the need for electrolyte optimization with respect to new solvents and additives (i.e.: FEC, VC, 1–3 PS)<sup>[51,52]</sup> becomes evident.

### 3. Conclusions

This study demonstrates the solvent-free processing of commercial NFM to cathodes with 1 wt.% PTFE binder which is reported for the first time, paving the way to a cost-efficient and NMP-free scalable production technique like the DRYtraec® process. Using XRD and SEM characterization, the preservation of active material crystal structure and its morphology were shown throughout the processing. The produced cathode contains a remarkably low binder content of only 1 wt.% and an active material content of 96 wt.%, thus reducing the amount of passive materials. A further reduction of the production footprint could be realized by the combination with an aqueous-processed HC anode yielding full-cells on coin-cell and pouch-cell level utilizing a NaPF<sub>6</sub> salt in EC/DEC electrolyte. The comparison to state-of-the-art wet-processed cathodes based on the critical NMP solvent reveal a high performance compared to the solvent-free processed cathode on coin-cell level. A comparable rate performance up to 2 C (81% compared to 0.05 C) towards a fully wet-processed full-cell reference was

demonstrated. Higher C-rates show a reduced rate capability that was caused by the compaction of electrode films without additional calendering step, indicating the need for further investigation of the relation between electrode compaction and cell performance by a calendering study.

At the same time, the degradation of full-cells based on dry-processed cathodes was found to be comparable to the wet-processed reference. However, first cycle capacity losses and a comparable steady degradation for both electrodes revealed limitations.

Finally, single-layered pouch-cells with commercially relevant electrode loadings of 2.7 mAh cm<sup>-2</sup> and 2.4 mAh cm<sup>-2</sup> were manufactured and demonstrated to reach up to 400 cycles until 80% end-of-life and an energy density of 102 Wh kg<sup>-1</sup>. Based on post-mortem analyses using SEM-EDX, the degradation was linked to local plating of sodium metal on the anode. Latter was linked to the presence of cathode active material species within the anode solid electrolyte interface (SEI). These findings reveal a dissolution and migration of transition metal ions for NFM and thereby the need for improved electrolyte compositions.

Overall, these first prototypes demonstrate a successful transition from wet-processing towards dry-processing of SIB cathodes via DRYtraec® process. However, the production of optimized SIB multi-layer pouch-cells requires the study of

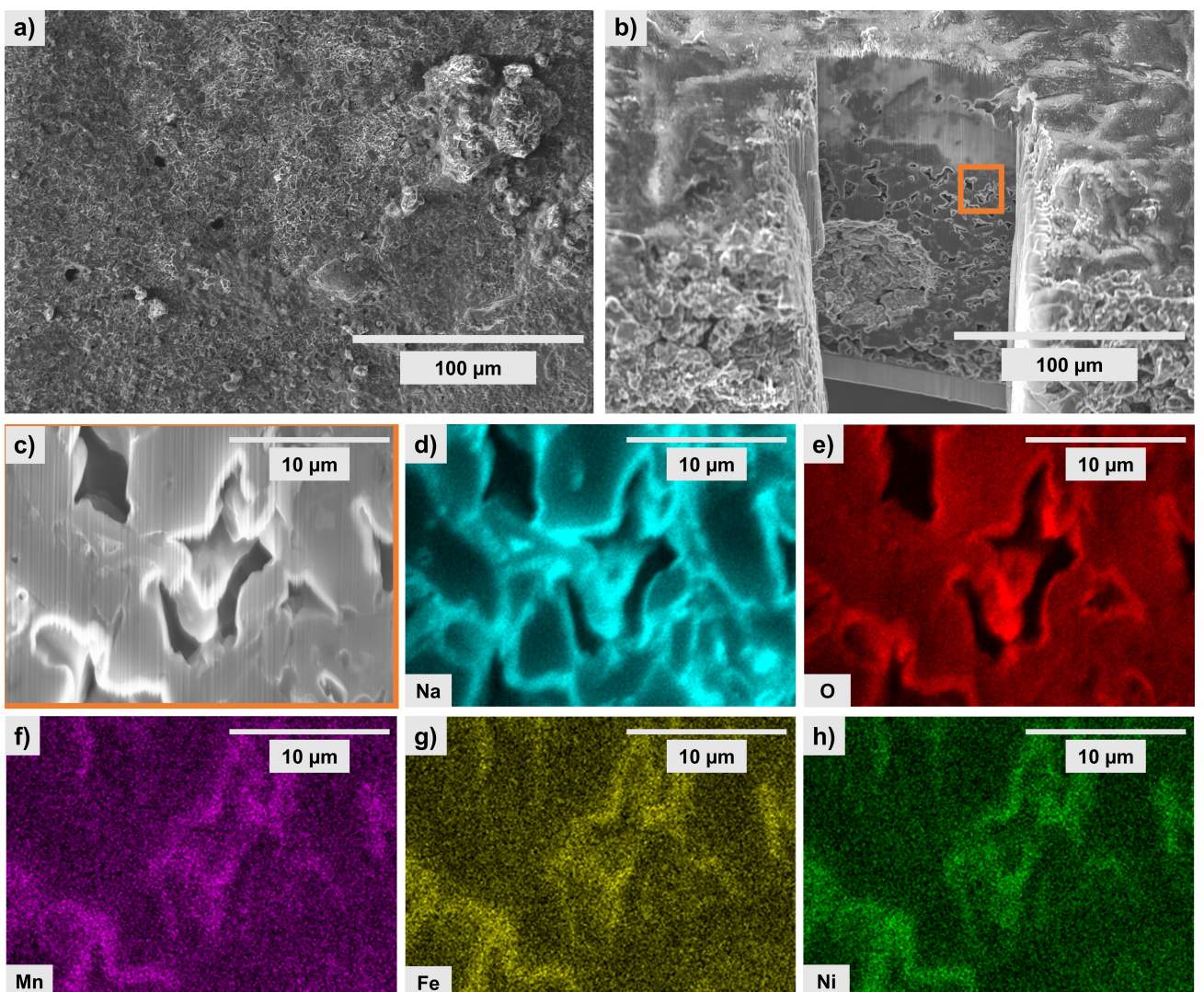


**Figure 6.** SEM micrograph of anode extracted after 400 cycles with partial sodium metal plating (a) and FIB cutting of area with strongest metal plating (b) as well as enlarged cross section marked by orange frame (c). EDX results of the enlarged cross section for sodium, oxygen, manganese, iron and nickel (c-h).

electrode density and fabrication of double-sided electrodes as well as new electrolyte formulation based on this proof-of-concept. In this way, the cost for production was decreased whereas the production footprint was reduced. Further research and development with respect to electrode density and electrolyte composition are desirable to promote a higher sustainability and performance of this technology with respect to energy density.

## Experimental Section

### Cathode Fabrication

The layered transition metal oxide-based dry-processed cathodes were prepared using the patented DRYtraec® process.<sup>[24,25]</sup> The dry-cathode composite was yielded by blending NFM (BN-P2B, BTR New Material Group Co., Ltd.), conductive carbon (Super C65, Imerys S.A.), multi-walled carbon nanotubes (Nanocyl 7000, Nanocyl S.A.), and high molecular weight emulsion polymerized PTFE in a

ratio of 96/2/1/1 with a blade mill (M20 Universal mill; IKA-Werke GmbH & Co. KG). The composite preparation and cathode fabrication, with the respective calender system, were conducted in a nitrogen-filled glovebox (dew point:  $-55^{\circ}\text{C}$ , Fraunhofer IWS). The electrode films were formed by applying shearing modulus by differential roll speed with a production capacity of  $2\text{ m min}^{-1}$ . A process temperature of  $110^{\circ}\text{C}$  and a hydraulic pressure of 240 bar were applied. The generated film was laminated onto a primer aluminium current collector foil ( $18\text{ }\mu\text{m Al}$  including  $1\text{ }\mu\text{m}$ ). The target loadings were  $19.8\text{ mg cm}^{-2}$  and  $24.3\text{ mg cm}^{-2}$  which equates to an areal capacity of  $2.3\text{ mAh cm}^{-2}$  and  $2.7\text{ mAh cm}^{-2}$ , respectively. For comparison, a wet-processed cathode was produced in a composition of 96/2/1/1 wt.% utilizing the same active material and conductive additives. The PTFE binder was replaced by a state-of-the-art PVDF (PVDF 7200, Kureha Corp.) dissolved in NMP (99.8%, Roth). An oscillating mill (MM-400, Retsch) was selected for mixing, with the use of five steel balls (10 mm) and a frequency of 10 Hz for 10 min for powder mixing. Once the binder-solvent solution was added, another mixing at 25 Hz for 10 min was applied. The resulting suspension was cast onto a primer aluminum current collector foil ( $18\text{ }\mu\text{m Al}$  including  $1\text{ }\mu\text{m primer}$ ) using a doctor blade (ZUA 2000, Zehntner Testing Instruments) and a

speed of  $50 \text{ mm s}^{-1}$  (Model 510, Ericson). The cathodes were dried at  $110^\circ\text{C}$  under nitrogen for 15 min in an oven (Thermo Fisher Scientific) and then transferred to vacuum.

Adhesion strength was determined for mechanical characterization using a uniaxial material testing machine (2.5 kN ZwickiLine, Zwick GmbH & Co. KG) with bond tester sample holder (Zwick GmbH & Co. KG). Therefore five measurements of 15 mm electrode discs were conducted with 20 Hz data acquisition rate under force control. A 12 mm adhesive tape disc was pressed on the sample with 70 N compression force with  $4 \text{ mm min}^{-1}$  for 10 s dwell time and a pull-off velocity of 4 mm/min.

### Anode Fabrication

In the case of the wet-processed reference anode, the as-received Kuranode Type 2 ( $9 \mu\text{m}$ ) hard carbon (Kuraray Co., Ltd.) was combined with a modified SBR binder (SSBR 100, Targray) and a CNF conductive additive (Pyrograf III®, Pyrograf Products Inc.) in a ratio of 90/5/5 wt%. The powders were mixed by oscillatory milling (MM-400, Retsch) using a 50 ml crucible with five steel balls (d: 10 mm) and a frequency of 10 Hz for 10 min. Subsequently, a further step at a frequency of 25 Hz for 10 min was used after the addition of the solvent. The suspension was then cast onto a primer aluminum current collector foil ( $18 \mu\text{m}$  Al including  $1 \mu\text{m}$ ) using a doctor blade (ZUA 2000, Zehntner Testing Instruments) at a speed of  $50 \text{ mm s}^{-1}$  (Model 510, Ericson). For electrode drying, an oven (Thermo Fisher Scientific) under atmosphere at  $110^\circ\text{C}$  was employed. The active material loading of hard carbon anodes fabricated was  $7.8 \text{ mg cm}^{-2}$ , while their areal capacity was  $2.6 \text{ mAh cm}^{-2}$ . For comparison, a higher loading of  $9.2 \text{ mg cm}^{-2}$  and  $3.0 \text{ mAh cm}^{-2}$  was prepared as well.

### Surface Morphology

The surface of the produced electrodes and during post-mortem analysis were examined via SEM and EDX. All samples were affixed to the sample holder with an adhesive carbon. Air-sensitive samples were transported to a FIB/SEM instrument (JIB 4610 JOEL Ltd.) using a transfer chamber developed in-house. The FIB cross-sections were created by bombarding the sample surface with gallium ions. An acceleration voltage of 5 kV and a working distance of 14 mm were employed. The recording angle was set at  $53^\circ$ . Additionally, the surface morphology of the electrodes was characterized using SEM. These measurements were conducted using a JSM 7800 (JEOL Ltd) instrument, with an acceleration voltage of 5 kV. The working distance was 4.5 mm.

### X-ray Diffraction

X-ray diffraction (XRD) patterns for the NFM samples were recorded on an Empyrean-3 Alpha 1 system X-Ray diffractometer with a Cu  $K_{\alpha 1}$  anode ( $\lambda = 0.154056 \text{ nm}$ ) operating at 40 kV and 40 mA in Bragg-Brentano reflection geometry. The diffraction patterns were collected at  $25^\circ\text{C}$  and over an angular range of  $5^\circ$  to  $70^\circ$ . The applied reflex free silicon wafer was covered with Kapton tape to protect the sample from fast degradation.

### Electrochemical Characterization

#### Half-Cell Tests

Prior to cell assembly, electrode discs with a diameter of 18 mm were subjected to vacuum drying at  $110^\circ\text{C}$  for 12 h. A three-

electrode setup (ECC-Ref, EL-CELL) was assembled in an argon-filled glovebox (MBraun) under conditions of  $< 0.1 \text{ ppm O}_2$  and  $\text{H}_2\text{O}$ . A glass fiber separator (thickness:  $1500 \mu\text{m}$ ; diameter: 18 mm), a sodium composite chip counter-electrode (thickness:  $420 \mu\text{m}$  Na and  $30 \mu\text{m}$  Al; diameter: 15.6 mm; AOT battery) and a sodium metal rod reference punched from sodium metal cubes (99.9% Na; Sigma Aldrich) were employed in the assembly of cells. Prior to sealing,  $350 \mu\text{L}$  electrolyte was added. A commercially available mixture of ethylene and diethylene carbonate (EC/DEC 4/6 v:v) with 1 M  $\text{NaPF}_6$  was employed as the electrolyte (E-Lyte Innovation GmbH). Prior to cell assembly, 5 wt.% FEC (99.9%, Solvionic) was added. Following assembly, the cells were allowed to rest for a period of 12 h at  $25^\circ\text{C}$ . The electrochemical characterization was conducted at a constant temperature of  $25 \pm 2^\circ\text{C}$  using a Biologic VMP-3 system (Biologic). Galvanostatic cycling was conducted with a constant current rate of 0.05 C within a voltage window from 0 V to 1.5 V for anodes ( $1 \text{ C} = 330 \text{ mAh g}^{-1}$ ) and from 2.0 V to 4.1 V for cathodes ( $1 \text{ C} = 115 \text{ mAh g}^{-1}$ ) in relation to  $\text{Na}/\text{Na}^+$  using potential control by the working electrode against reference (Ewe-Ref). A high resolution of  $dQ/dV$  graphs was ensured by setting the voltage registration criterion to 1 mV. Each measurement was conducted using a double determination.

For electrochemical impedance spectroscopy, the same cell-setup was applied. The measurement was conducted under constant temperature of  $25 \pm 2^\circ\text{C}$  using a Biologic VMP-3 system (Biologic). For the formation, two cycles at constant current rate of 0.05 C within a voltage window 2.0 V to 4.1 V ( $1 \text{ C} = 115 \text{ mAh g}^{-1}$ ) in relation to  $\text{Na}/\text{Na}^+$  using potential control by the working electrode against reference (Ewe-Ref) was applied. After formation the cells were cycled at 0.1 C for 25 cycles with a check-up cycle after 5 cycles. During the check-up cycle a PEIS configuration under cell voltage potential control (Ewe-Ece) was used. A range from 1 MHz to 1 Hz was applied with an amplitude of 20 mV and 10 points per decade in logarithmic spacing with 2 averaged measures per frequency. The cathode potential was held at 2.0 V before measurement corresponding to 100% SOC.

#### Full-Cell Tests

The electrodes for full-cell measurement were first punched out to a diameter of 16 mm and 15 mm for the HC anode and NFM cathode, respectively. Prior to cell assembly, the electrodes were dried at  $110^\circ\text{C}$  under vacuum for 12 h. NFM vs. HC full-cells were constructed as CR2016 coin-cells in an argon-filled glovebox (MBraun, conditions:  $< 0.1 \text{ ppm O}_2$  and  $\text{H}_2\text{O}$ ) using a  $25 \mu\text{m}$  PP separator and  $100 \mu\text{L}$  of the electrolyte. The electrolyte utilized was the aforementioned ethylene and diethylene carbonate (EC/DEC 4/6 v:v) with 1 M  $\text{NaPF}_6$  and without FEC. Prior to testing, the cells were allowed to rest for 12 h at  $25^\circ\text{C}$ . Electrochemical tests were conducted at  $25 \pm 2^\circ\text{C}$  with a BaSyTec cell testing system (BaSyTec GmbH, Germany) in a voltage range between 1.5 V and 4.1 V. The formation of the cells was achieved through three cycles of 0.05 C CCCV (0.025 C) and 0.05 C CC discharge. Subsequently, ten additional cycles were conducted at 0.1 C. Following the thirteenth cycle, an asymmetric rate capability test was performed with a constant charge rate of 0.3 C CCCV (0.05 C) and CC steps with discharge rates of 0.5 C, 1 C, 2 C and 3 C for three cycles, each. For the long-term cycling, a charging rate of 0.3 C CCCV (0.05 C) and 0.5 C for discharge was selected until 80 cycles. A triple determination was employed.

Pouch-cells were assembled using a single-sided anode, single-sided cathode,  $25 \mu\text{m}$  PP separator and 1 mL ( $13.0 \mu\text{L mAh}^{-1}$  and  $14.8 \mu\text{L mAh}^{-1}$ ) electrolyte (1 M  $\text{NaPF}_6$  in EC/DEC 4/6 v:v + 2 wt% 1,3-PS). The cell manufacturing process was conducted in an argon-filled glovebox (MBraun, conditions:  $< 0.1 \text{ ppm O}_2$  and  $\text{H}_2\text{O}$ ). An

external uniaxial pressure of 0.076 MPa was applied during the cycling process and was controlled by a pneumatic regulator (Fraunhofer IWS). The cell tests were conducted on a BaSyTec cell testing system (BaSyTec GmbH, Germany). In order to accomplish initial formation, a current of 0.05 C CCCV (0.025 C) for charge and 0.05 C CC for discharge was applied in a voltage window of 1.5–4.1 V for four cycles. Following the formation, the upper voltage limit was lowered to 4.0 V. An asymmetric rate capability test was then performed with a constant charging current of 0.3 C CCCV (0.05 C), while the CC discharge rates were 0.1 C, 0.5 C, 1 C and 2 C, respectively, for three cycles. During long-term cycling, a current rate of 0.3 C CCCV (0.05 C) for charging and 0.5 C for discharging the cell was selected. The cells were subjected to continuous cycling until they reached the end-of-life criterion of 80% of their initial charge capacity. All measured specific capacities were related to the mass of active material.

## Acknowledgements

The authors acknowledge the support by gained experience from the project “Development and Testing of Ultra-light Composite Structures with Integrated Electrical Storage Function” (EIVIS), funding code 20E2118C, financed by the Federal Ministry for Economic Affairs and Climate Action on the basis of a decision by the German Bundestag. Additionally, this work have been made possible with the funding provided by Technical University Dresden and Fraunhofer IWS Advanced Battery Technology Center. Furthermore the author thank Dr. Jörg Bretschneider and Anja Mittag for the SEM and FIB-SEM characterization of the electrodes as well as Dr. Tom Boenke for the preparation of aqueous-processed reference electrodes. Finally, Florian Hoffmann and Paul Härtel for the production and characterization of pouch-cells. Open Access funding enabled and organized by Projekt DEAL.

## Conflict of Interests

The authors declare no conflict of interest.

## Data Availability Statement

The data that support the findings of this study are available from the corresponding author upon reasonable request.

**Keywords:** batteries · sodium-ion · full-cell · pouch-cell · NFM · solvent-free · dry-coating

- [1] B. Jones, V. Nguyen-Tien, R. J. R. Elliott, *World Economy* **2023**, *46*, 2.
- [2] R. J. Brodd, in *Lithium-Ion Batteries* (Eds.: M. Yoshio, R. J. Brodd, A. Kozawa), Springer New York, New York, NY **2009**, p. 1.
- [3] B. Diouf, R. Pode, *Renewable Energy* **2015**, *76*, 375.
- [4] Q. Liu, R. Xu, D. Mu, G. Tan, H. Gao, N. Li, R. Chen, F. Wu, *Carbon Energy* **2022**, *4*, 458.
- [5] D. Chung, E. Elggqvist, S. Santhanagopalan, *Automotive Lithium-ion Cell Manufacturing: Regional Cost Structures and Supply Chain Considerations* **2016**.
- [6] M. Kotal, S. Jakhar, S. Roy, H. K. Sharma, *J. Energy Storage* **2022**, *47*, 103534.
- [7] S. Dörfler, H. Althues, P. Härtel, T. Abendroth, B. Schumm, S. Kaskel, *Joule* **2020**, *4*, 539.
- [8] *Mineral commodity summaries 2023* **2023**.
- [9] E. R. Sadik-Zada, A. Gatto, M. Scharfenstein, *Technol. Forecast. Soc. Change* **2023**, *186*, 121992.
- [10] J.-Y. Hwang, S.-T. Myung, Y.-K. Sun, *Chem. Soc. Rev.* **2017**, *46*, 3529.
- [11] R. J. Clément, P. G. Bruce, C. P. Grey, *J. Electrochem. Soc.* **2015**, *162*, A2589–A2604.
- [12] P. K. Nayak, L. Yang, W. Brehm, P. Adelhelm, *Angew. Chem. Int. Ed.* **2018**, *57*, 102.
- [13] J. Ge, L. Fan, A. M. Rao, J. Zhou, B. Lu, *Nat Sustain* **2022**, *5*, 225.
- [14] A. M. Skundin, T. L. Kulova, A. B. Yaroslavtsev, *Russ. J. Electrochem.* **2018**, *54*, 113.
- [15] G. B. Haxel, J. B. Hedrick, G. J. Orris, P. H. Stauffer, J. W. Hendley, *Fact Sheet* **2002**.
- [16] C. Delmas, *Adv. Energy Mater.* **2018**, *8*, 1703137.
- [17] K. Kubota, S. Komaba, *J. Electrochem. Soc.* **2015**, *162*, A2538–A2550.
- [18] C. Vaalma, D. Buchholz, M. Weil, S. Passerini, *Nat. Rev. Mater.* **2018**, *3*, 18013.
- [19] L. Wang, J. Hu, Y. Yu, K. Huang, Y. Hu, *J. Cleaner Prod.* **2020**, *276*, 124244.
- [20] B. Schumm, S. Kaskel, *Next Energy* **2023**, *1*, 100009.
- [21] F. Degen, O. Krätzig, *IEEE Trans. Eng. Manage.* **2024**, *71*, 1038.
- [22] J. Klemens, A.-K. Wurba, D. Burger, M. Müller, W. Bauer, S. Büchele, O. Leonet, J. A. Blázquez, I. Boyano, E. Ayerbe, H. Ehrenberg, J. Fleischer, A. Smith, P. Scharfer, W. Schabel, *Batteries & Supercaps* **2023**, *6*, e20230091.
- [23] M. Ni, Y. Zhao, N. Xu, M. Kong, Y. Ma, C. Li, H. Zhang, Y. Chen, *Sci. China Mater.* **2024**, *67*, 76.
- [24] J. Brückner, S. Tschocke, H. Althues, S. Kaskel, S. Thieme, (Fraunhofer Gesellschaft zur Förderung der Angewandten Forschung eV Technische Universität Dresden), DE102012203019 A1, H01M4/04;H01M4/139; H01M4/62 **2013**.
- [25] S. Tschocke, H. Althues, B. Schumm, S. Kaskel, C. Schult, D. Fritsche, K. Schönher, (Fraunhofer Gesellschaft zur Förderung der Angewandten Forschung eV Technische Universität Dresden), DE102017208220 A1, **2017**.
- [26] F. Hippauf, B. Schumm, S. Doerfler, H. Althues, S. Fujiki, T. Shiratsuchi, T. Tsujimura, Y. Aihara, S. Kaskel, *Energy Storage Mater.* **2019**, *21*, 390.
- [27] M. Fiedler, S. Cangaz, F. Hippauf, S. Dörfler, T. Abendroth, H. Althues, S. Kaskel, *Adv. Sustainable Syst.* **2023**, *7*, 2200439.
- [28] F. Schmidt, S. Kirchhoff, K. Jägle, A. De, S. Ehrling, P. Härtel, S. Dörfler, T. Abendroth, B. Schumm, H. Althues, S. Kaskel, *ChemSusChem* **2022**, *15*, e202201320.
- [29] F. Schmidt, M. Fiedler, T. Arlt, A. De, F. Hoffmann, F. Wilde, S. Dörfler, B. Schumm, T. Abendroth, H. Althues, S. Kaskel, *Energy Technol.* **2023**, *11*, 2300518.
- [30] D. Chen, C. Hu, Q. Chen, G. Xue, L. Tang, Q. Dong, B. Chen, F. Zhang, M. Gao, J. Xu, Y. Shen, L. Chen, *Nano Res.* **2023**, *16*, 3847.
- [31] C. Fang, Y. Huang, W. Zhang, J. Han, Z. Deng, Y. Cao, H. Yang, *Adv. Energy Mater.* **2016**, *6*, 1501727.
- [32] M. Abdollahifar, H. Cavers, S. Scheffler, A. Diener, M. Lippke, A. Kwade, *Adv. Energy Mater.* **2023**, *13*, 2300973.
- [33] S. Jia, S. Kumakura, E. McCalla, *Energy Environ. Sci.* **2024**, *17*, 4343.
- [34] T. Lan, W. Wei, S. Xiao, G. He, J. Hong, *J. Mater. Sci. Mater. Electron.* **2020**, *31*, 9423.
- [35] T. Chen, W. Liu, H. Gao, Y. Zhuo, H. Hu, A. Chen, J. Zhang, J. Yan, K. Liu, *J. Mater. Chem. A* **2018**, *6*, 12582.
- [36] Y. Wang, S. Kim, J. Lu, G. Feng, X. Li, *Batteries & Supercaps* **2020**, *3*, 376.
- [37] R. Dugas, J. D. Forero-Saboya, A. Ponrouch, *Chemistry of Materials Chem. Mat.* **2019**, *31*, 8613.
- [38] C. Müller, Z. Wang, A. Hofmann, P. Stüble, X. Liu-Théato, J. Klemens, A. Smith, *Batteries & Supercaps* **2023**, *6*, e202300322.
- [39] D. Yuan, X. Hu, J. Qian, F. Pei, F. Wu, R. Mao, X. Ai, H. Yang, Y. Cao, *Electrochim. Acta* **2014**, *116*, 300.
- [40] J. Deng, W.-B. Luo, S.-L. Chou, H.-K. Liu, S.-X. Dou, *Adv. Energy Mater.* **2018**, *8*, 1701428.
- [41] I. Hasa, S. Mariyappan, D. Saurel, P. Adelhelm, A. Y. Koposov, C. Masquelier, L. Croguennec, M. Casas-Cabanas, *J. Power Sources* **2021**, *482*, 228872.
- [42] S. Komaba, T. Ishikawa, N. Yabuuchi, W. Murata, A. Ito, Y. Ohsawa, *ACS Appl. Mater. Interfaces* **2011**, *3*, 4165.
- [43] G. Yan, R. Dugas, J.-M. Tarascon, *J. Electrochem. Soc.* **2018**, *165*, A220–A227.

- [44] P. Stüble, C. Müller, J. Klemens, P. Scharfer, W. Schabel, M. Häringer, J. R. Binder, A. Hofmann, A. Smith, *Batteries & Supercaps* **2024**, *7*, e202300375.
- [45] X. Jiang, T. Zhang, J. Y. Lee, *J. Power Sources* **2017**, *372*, 91.
- [46] A. Barai, K. Uddin, M. Dubarry, L. Somerville, A. McGordon, P. Jennings, I. Bloom, *Prog. Energy Combust. Sci.* **2019**, *72*, 1.
- [47] J. Martínez De llarduya, L. Otaegui, M. Galcerán, L. Acebo, D. Shanmukaraj, T. Rojo, M. Armand, *Electrochim. Acta* **2019**, *321*, 134693.
- [48] M. F. C. Millares, E. S. Takeuchi, K. J. Takeuchi, A. C. Marschilok, D. C. Bock, *MRS Advances* **2023**, *8*, 381.
- [49] C. Constable, F. Coowar, M. Copley, E. Kendrick, C. Dancer, I. Hasa, *J. Electrochem. Soc.* **2024**, *171*, 23506.
- [50] T. Qin, H. Yang, Q. Li, X. Yu, H. Li, *Ind. Chem. Mater.* **2024**, *2*, 191–225.
- [51] H. Che, X. Yang, H. Wang, X.-Z. Liao, S. S. Zhang, C. Wang, Z.-F. Ma, *J. Power Sources* **2018**, *407*, 173.
- [52] A. Nimkar, N. Shipigel, F. Malchik, S. Bublil, T. Fan, T. R. Penki, M. N. Tsubery, D. Aurbach, *ACS Appl. Mater. Interfaces* **2021**, *13*, 46478.

---

Manuscript received: September 10, 2024

Revised manuscript received: January 20, 2025

Accepted manuscript online: January 25, 2025

Version of record online: February 5, 2025

---